On the Role of Crystallographic Anisotropy and Texture in Damage Tolerance of Magnesium and Its Alloys

Shahmeer Baweja, Padmeya P. Indurkar, and Shailendra P. Joshi

Abstract

The remarkable crystallographic plastic anisotropy of magnesium and its alloys reflects in its polycrystal response via texture. While texture-strength linkages have been studied, the role of textural variability on damage remains elusive. The challenge is to obtain relevant metrics that relate the net plastic anisotropy to macroscopic modes of damage. A possible approach is to adopt mechanistic descriptions of the damage. Motivated by the recent experimental and theoretical works in this direction, here we appeal to the Hill yield function to characterize the net plastic anisotropy of polycrystalline magnesium via the Hill plastic anisotropy tensor $\mathbb{h}$. Metrics based on the components of $\mathbb{h}$ offer a way to predict damage as a possible damage predictor. Using the results from our recent extensive three-dimensional crystal plasticity simulations for a wide range of textures, we map the net plastic anisotropy on to the coefficients of $\mathbb{h}$, separately for the tensile and compressive responses. Metrics based on these coefficients serve as indicators for the propensity of textured polycrystals to damage by: (i) porosity evolution, or (ii) shear instability. An attempt is made to understand the potential roles textural variability and crystallographic plastic anisotropy play in damage under different loading conditions.

Keywords

HCP materials • Damage tolerance • Textural variability • Plastic anisotropy • Crystal plasticity

S. Baweja · S. P. Joshi (✉)
Department of Mechanical Engineering, University of Houston, Houston, TX 77204-4006, USA
e-mail: shailendra@uh.edu

P. P. Indurkar
Department of Mechanical Engineering, National University of Singapore, Singapore, 117575, Singapore

Introduction

It is recognized that ductile failure is a multi-scale phenomenon [1, 2]. Crystallography defines deformation mechanisms at the atomic scale, which interact with microstructural length-scales defined by the size and distribution of microscopic defects (e.g. second-phase particles) to trigger damage through void nucleation and growth. Coarser length-scales appear with inter-flaw interactions that ultimately coalesce to form mesoscopic damage zones. Interaction of meso-scale structures with specimen/component scale forms the final feature of macroscopic failure. Coupling between these length-scales is often complicated by the anisotropic nature of plasticity but is of particular significance in hexagonal close-packed (HCP) materials that deform by protean slip and twinning mechanisms.

The remarkable crystallographic plastic anisotropy, tension-compression asymmetry, and strong texture effects exhibited by many HCP materials are often referred to as origins of damage intolerance. Their plastic anisotropy and strength asymmetry are a result of intricate slip and twinning mechanisms [3–5]. Such materials also tend to exhibit more complex damage evolution [6–8]. Huez et al. [9] reported void evolution at twins, twin-twin intersections, and twin-particle intersections in an α-Ti alloy under different triaxiality levels with unexpectedly rapid growth rates. Crépin [6] and Caré [10] observed hexagonal shaped tubular dimples in Zr alloys, attributed to the prismatic slip. More recent investigations on single [7] and alloyed polycrystals [11, 12] of Mg, as well as on Ti alloys [13] serve as potent markers for the need to assess the role of slip and twinning on anisotropic ductile damage.

Recent experiments on two dilute solute-strengthened Mg alloys (AZ31B and WE43) with different levels of plastic anisotropy reveal the following salient characteristics [14, 15]: (i) a non-monotonic dependence of fracture strain on the stress state, (ii) a strong effect of the stress triaxiality on the

V. M. Miller et al. (eds.), *Magnesium Technology 2021*, The Minerals, Metals & Materials Series,
https://doi.org/10.1007/978-3-030-65528-0_14

forensics of fracture ranging from quasi-brittle (cleavage-like) to ductile (dimpled) features on fracture surfaces, and (iii) a dramatic dependence of the tensile ductility on the level of plastic anisotropy. Quasi-brittle fracture with the linkage of twin induced microcracks in WE43 versus more ductile fracture AZ31B via void linkage alludes to the role of alloying and texture-induced plastic anisotropies on ultimate fracture [12]. Even for the same material (AZ31B), subjected to similar loading conditions, contrasting observations on the nature of damage mechanisms viz. micro-void sheeting [16] versus micro-void growth and coalescence [11], present an intriguing dichotomy. This is apparent even in single crystals where synergistic correlation between $\{10\bar{1}2\}$ extension twinning and toughness [7] conflicts with the low toughness and ductility associated with twinning [4, 5].

Another critical aspect that remains unresolved in our understanding of damage in HCP materials is the role of plastically soft slip and twinning mechanisms in shear failure. This is important for several reasons: first, shear failure may set limits to ductility that are more severe than by mere damage accumulation (void growth to coalescence) [17]. Second, experiments indicate that damage in the form of flattened micro-voids (at twins or second-phase particles) remains relatively flat as damage evolves, in contrast with continuum porous metal plasticity models, which predict significant blunting of such initial penny-shaped voids [18]. Uniaxial tensile experiments using flat tapered tensile specimens of an Mg rare-earth alloy (ZEK100) with AZ31B alloy [12] reveal that while the ZEK100 exhibits a quasi-brittle (flat fracture surface) failure compared to the more ductile (dimpled) characteristics in AZ31B, the final failure occurs via macroscopic shear localization in both alloys.

These experimental observations hint at more complex interactions between plastic anisotropy and failure mechanisms than currently appreciated. On the sole basis of experiments, it is unclear how, and to what extent, matrix plastic anisotropy affects the rates and states of damage accumulation in structural components. Computational investigations of boundary value problems based on damage-free polycrystal plasticity modeling [19] as well as those based on homogenization-based porous plasticity [17] shed some light in this regard. For failure induced by internal damage accumulation via porosity evolution of Hill-type anisotropic materials, a so-called AED (anisotropy effect on ductility) index has been proposed [20, 21]. On the other hand, Benzerga et al. [17] indicate that shear failure is plausible even in geometries and under tensile boundary conditions that are stiff against the formation of shear bands, and that the net plastic anisotropy may be the main driving factor for shear fracture. In particular, the role of shear anisotropy ratios may be important, although a robust index (akin to the AED index) characterizing their role in shear fracture remains elusive.

The foregoing concepts of the AED index and, to some extent, the shear anisotropy ratios, have been shown to corroborate well with broader experimental observations on materials exhibiting Hill-type plastic anisotropy [17, 20]. On that backdrop, Mg and its alloys cannot be well described by a Hill-type yield function owing to the tension-compression asymmetry as a result of the polar nature of twinning. Nevertheless, the recent analysis of Mg alloys based on these ideas [21] suggests it may still provide a useful basis for a theory-based design paradigm of damage-tolerant HCP materials. Hence, it serves as a motivation for the present analysis.

In this work, we view the role of *net* plastic anisotropy that embeds the intrinsic (crystallographic) and textural effects on the potential macroscopic damage modes in HCP materials with a focus on Mg alloys. In particular, we attempt to address the following questions in the context of Mg and its alloys:

1. How do crystallographic and textural effects influence the AED index and shear anisotropy ratios under tensile and compressive loading? An allied question is: to what extent do the differences in these metrics computed from tensile versus compressive loading qualitatively affect the broader conclusions?
2. Are there combinations of crystallographic and texture-induced plastic anisotropy (hereafter referred to as the net plastic anisotropy) that satisfy minimum requirements for a material to be potentially damage-tolerant?

To address these questions, we rely on the dataset from our recent three-dimensional crystal plasticity investigation on polycrystal statistical volume elements (SVEs) performed for a range of synthetic textures that mimic experimental rolling textures at two different levels of crystallographic plastic anisotropies [22]. The explicit resolution of the SVE combined with crystallographic kinetics of plasticity provides detailed insight into the evolution of microstructure-property linkages including plastic anisotropy and tension-compression asymmetry [22].

Computational Setup

A detailed account of the three-dimensional crystal plasticity modeling and simulation of the polycrystalline SVE is provided in Ref. [22]. It considers eleven textures and two crystallographic plastic anisotropies (one representing an Mg alloy and the other representing pure Mg). For each texture, we perform simulations under uniaxial stress condition along six directions: (i) three along material principal axes (L, T, S), and (ii) three off-axes (LT, LS, TS), characterizing the full macroscopic plastic anisotropy for each microstructure. Moreover, to characterize the tension-compression asymmetry, monotonic uniaxial compressive and tensile loading states are applied. Thus, for each crystallographic plastic anisotropy, we perform 132 simulations.

The present work builds upon those detailed calculations with a focus on characterizing the role of net plastic anisotropy in the potential damage response of Mg and its alloys. In what follows, we provide a brief background of the key microstructural descriptors that are adopted in the discussion of the results.

Texture Descriptor

In the polycrystal plasticity simulations, we create three-dimensional Voronoi tessellations of a cubic domain in NEPER [10], giving in an SVE with 300 grains ($N_{grains} = 300$) that are discretized into a fine finite element mesh. The discretized SVE is imported into ABAQUS/STANDARD® for subsequent mechanical analysis. To describe a texture of an SVE, individual grains are characterized by distinct Euler angle sets in the Bunge representation: $[E] = \left[\overline{\varphi}_1 \pm \varphi_1^{\sigma}, \overline{\Phi} \pm \Phi^{\sigma}, \overline{\varphi}_2 \pm \varphi_2^{\sigma}\right]$ where $[\overline{\varphi}_1, \overline{\Phi}, \overline{\varphi}_2]$ denote the mean values and $\varphi_1^{\sigma}, \Phi^{\sigma}, \varphi_2^{\sigma}$ their respective standard deviations. Using a normal distribution with $\overline{\varphi}_1 = \overline{\Phi} = \overline{\varphi}_2 = 0$, each texture is then described by the maximum standard deviation $[E^{\sigma}] = [\varphi_1^{\sigma}, \Phi^{\sigma}, \varphi_2^{\sigma}]$.

Under a uniaxial loading controlled via applied nominal strain rate $\left(\dot{\varepsilon}_{app}\right)$, the macroscopic stress state in the SVE is $\boldsymbol{\Sigma} = \Sigma_{yy}\left(\boldsymbol{e}_y \otimes \boldsymbol{e}_y\right)$, where $\boldsymbol{e}_y$ is the unit vector in the y-direction (loading axis). The corresponding macroscopic logarithmic strain state is: $\mathbf{E} = \mathrm{E}_{xx}(\boldsymbol{e}_x \otimes \boldsymbol{e}_x) + \mathrm{E}_{yy}\left(\boldsymbol{e}_y \otimes \boldsymbol{e}_y\right) + \mathrm{E}_{zz}(\boldsymbol{e}_z \otimes \boldsymbol{e}_z)$where $\mathrm{E}_{xx} = \ln(L_x/L_0)$, $\mathrm{E}_{yy} = \ln\left(L_y/L_0\right)$, and $\mathrm{E}_{zz} = \ln(L_z/L_0)$. The von-Mises equivalent stress is: $\Sigma_{eq} = \sqrt{(3/2)\boldsymbol{\Sigma}' : \boldsymbol{\Sigma}'} = |\Sigma_{yy}|$ and the corresponding effective strain is: $\mathrm{E}_{eq} = \sqrt{(2/3)\mathbf{E}' : \mathbf{E}'}$ where $\boldsymbol{\Sigma}'$ are the deviatoric stresses and $\mathbf{E}'$ are the corresponding deviatoric strains. Finally, the macroscopic strain ratios (also known as the Lankford ratios) are given by: $R_L = \mathrm{E}_{TT}/\mathrm{E}_{SS}; R_T = E_{LL}/E_{SS}; R_{LT} = E_{LT^{\perp}}/E_{SS}; R_{LS} = E_{LS^{\perp}}/E_{TT}; R_{TS} = E_{LL}/E_{TS^{\perp}}$ [see [22] for further details].

HCP Crystal Plasticity

The finite strain crystal plasticity model comprises of eighteen slip systems (3 basal, 3 prismatic, 6 pyramidal $\langle a \rangle$, and 6 pyramidal $\langle c + a \rangle$) and twelve twin systems (6 extension twinning and 6 contraction twinning) with rate-dependent viscoplastic flow rules that embed the physics of plasticity kinetics and incorporate twinning-induced lattice reorientation [23]. Two sets of material parameters are considered (Table 2); one set of parameters is representative of an Mg alloy (AZ31B) and those in the brackets are for 99.97% pure Mg [22].

Micromechanical Theory of Anisotropic Damage

As noted earlier, the hypothesis underlying this work is that both, intrinsic plastic anisotropy and texture-induced effect play a role in the damage tolerance of Mg alloys. For a pristine (*damage-free*) material, these contributions emerge in the form of the net plastic anisotropy at the macroscopic scale, which may be characterized by one of the several anisotropic yield functions [24]. In this work, we choose a Hill-type representation of the net plastic anisotropy. Admittedly, such a representation may be deemed too simplistic for materials such as Mg that exhibit a complex plastic anisotropy and perhaps even inadequate as it does not cater for the tension-compression asymmetry [13]. Notwithstanding this caveat, the choice of this yield model is driven by two considerations. First, it is a simple representation of the plastic anisotropy that offers a physical basis to the anisotropy coefficients in the yield function. Second, the yield function has been extended to incorporate damage by porosity evolution [25]. These features make the theory attractive in gaining insights by correlating the coefficients of Hill anisotropy tensor to the two primary mechanisms of macroscopic ductile fracture: (i) internal damage accumulation by void growth, and (ii) mechanical instability driven by shear bands. Indeed, the trends based on this model have been shown to broadly corroborate with the experimentally observed ductility trends in some Mg alloys [21, 26]. Below, we briefly elucidate the main ingredients of the Hill plastic anisotropy and its relation to damage. For a Hill-type material, the yield condition is:

$$\sigma_{eq}^2 = \frac{3}{2}\mathbf{s} : \mathbb{h} : \mathbf{s} = \tilde{\sigma}^2$$

where σ_{eq} is the equivalent stress of the Hill yield criterion,$\mathbf{s}$ the stress deviator, $\mathbb{h}$ the fourth-order Hill anisotropy tensor, and $\tilde{\sigma}$ the flow stress. The flow stress is arbitrarily chosen along a direction, which serves as the reference direction. Referring to Fig. 1, with loading axes aligned with the principal directions of plastic orthotropy, the above equation reduces to:

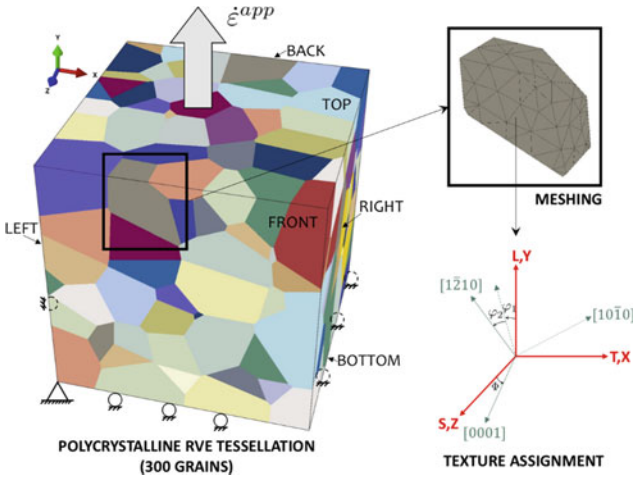

Fig. 1 Polycrystal SVE. The material directions are denoted by L, T, and S. Uniaxial loading is applied along the global y-axis. The particular case shown here is L-tension. (Color figure online)

$$\sigma_{eq}^2 = \frac{3}{2}\left(h_L s_{11}^2 + h_T s_{22}^2 + h_S s_{33}^2 + 2h_{LT} s_{12}^2 + 2h_{LS} s_{13}^2 + 2h_{TS} s_{23}^2\right) = \tilde{\sigma}^2 \tag{1}$$

the anisotropy coefficients h_i are related to those used by Hill [27]. In the present work, a strain-based approach is used in the calculation of these coefficients. Given the principal directions of plastic orthotropy L-T-S, the strain relationships between h_i and the strain ratios are as follows:

$$\frac{h_T}{h_L} = 1 - \frac{3(R_L R_T - 1)}{R_L R_T - 2R_L - 2}; \frac{h_s}{h_L} = 1 - \frac{3R_L(R_T - 1)}{R_L R_T - 2R_L - 2}; \frac{h_{LT}}{h_L} = -\frac{1}{2}\frac{(2R_{LT} + 1)(R_L R_T + 1)}{R_L R_T - 2R_L - 2}$$

$$\frac{h_{LS}}{h_L} = -\frac{1}{2}\frac{(2R_{LS} + 1)(R_L + 1)}{R_L R_T - 2R_L - 2}; \frac{h_{TS}}{h_L} = -\frac{1}{2}\frac{(2R_{TS} + 1)(R_L + 1)}{R_L R_T - 2R_L - 2}$$

These anisotropy coefficients enter in the micromechanics of damage via porosity evolution as follows [20]:

$$\frac{\dot{f}}{\dot{\varepsilon}_{eq} f} \approx \frac{3}{h}\sinh\left(\frac{3}{h}\mathcal{T}\right) \tag{2}$$

where f is the current void volume fraction, $\dot{\varepsilon}_{eq}$ is the effective plastic strain rate, $\mathcal{T}$ is the stress triaxiality ratio, and h is a scalar invariant of $\mathbb{h}$, given by:

$$h = 2\left[\frac{2}{5}\frac{h_L + h_T + h_S}{h_L h_T + h_T h_S + h_L h_S} + \frac{1}{5}\left(\frac{1}{h_{LT}} + \frac{1}{h_{LS}} + \frac{1}{h_{TS}}\right)\right]^{\frac{1}{2}} \tag{3}$$

Equation (2) shows that the rate of growth of porosity $\dot{f}$ in a plastically anisotropic material is a function of the *degree of plastic anisotropy*, characterized by h. As such, it is referred to as the Anisotropy Effect on Ductility (AED) index [21]. In the limiting case of plastic isotropy, all $h_i = 1$, which gives $h = 2$.

Another canonical mode of failure is the propensity to failure by mechanical instability via shear bands, referred to as shear failure. As expounded in Ref. [28], shear failure is distinct from failure in shear; while the former may occur under remote loading states devoid of a shear component, the latter occurs under dominant shear loading conditions. While there is no robust index (even for a Hill-type plastic anisotropy) yet that describes the propensity of a plastically anisotropic material to macroscopic shear failure, the role of plastic anisotropy in shear failure may to zeroth order, be viewed from the vantage point of the ratios of shear anisotropy coefficients [17]. In orthotropic plasticity, the coefficients of interest are h_{LS} and h_{TS}. We discuss this further in the next section.

Results and Discussion

In the following, we present the evolution and textural dependencies of three quantities computed from the expressions in the preceding section using the data from crystal plasticity simulations [22]. These quantities are: the AED index h (Eq. 3), and two shear anisotropy ratios $\widehat{h}_{LST} = h_{LS}/h_T$ and $\widehat{h}_{TSL} = h_{TS}/h_L$ (cf. Eq. 1). In what follows, we focus on the results for an Mg alloy (Table 2), and later comment on the role of crystallographic anisotropy by examining the trends for pure Mg (Section "Role of Crystallographic Anisotropy").

AED Index

Figure 2 shows the evolution of the AED index with equivalent strain E_{eq} calculated from tensile loading along the L, T, S, LT, LS, and TS directions as detailed in Ref. [22]. The different curves are for different textures ranging from A through K (cf. Table 1).

Beyond the initial transient, all curves show a systematic increase with a tendency toward steady-state values at large strains ($E_{eq} \sim 0.2$). The dashed line demarcates an isotropic plastic response. There is a dependence of h on texture. This is clearer from Fig. 3, which captures steady-state values of the AED index for each texture. For tensile loading, the steady-state values of the AED index are in the range $1.9 \lesssim h \lesssim 2.5$. Recall that for a plastically isotropic material

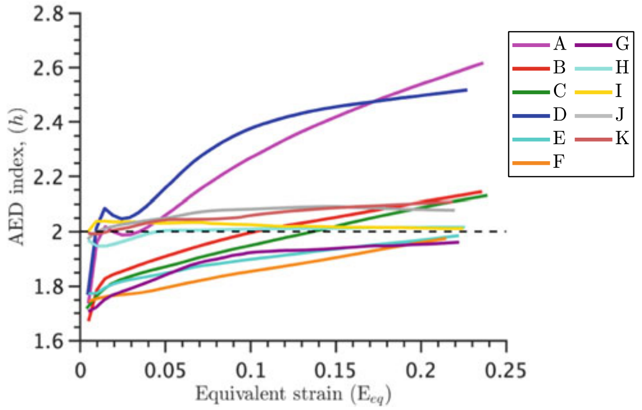

Fig. 2 Evolution of AED index with strain for different textures under tensile loading (Mg alloy). The dashed line indicates the limiting case of isotropic plasticity. (Color figure online)

$h = 2$. The AED index exhibits a non-monotonic correlation with the peak intensity of the (0001) pole figure. With reference to Table 1, textures with the highest and the lowest (0001) peak intensities show $h > 2$ with stronger textures showing higher values. In comparison, textures with intermediate (0001) peak intensities exhibit tempered values of $h \lesssim 2$. While the corresponding correlation with $\left(10\bar{1}0\right)$ peak intensities is not as clean, the trends are roughly similar. Broadly, it appears then that that stronger textures are likely to be more resistant to void growth than their weaker counterparts and isotropic materials.

A similar analysis using compression datasets along the same six directions allows computing AED indices, whose steady-state values are also shown in Fig. 3. For a Hill-type material (no tension-compression asymmetry), the AED index calculated from the compression data should be identical to its tensile counterpart. In such a scenario, the choice of compressive tests is driven by practical considerations; they are more cost-effective and consume less material per test. For most Mg alloys, the tension-compression asymmetry precludes the use of the AED index computed from the compression dataset. As seen from Fig. 3, the *compressive* AED indices lie below the isotropic limit whereas the *tensile* AED indices indicate a more sensitivity to textural variations. For instance, given a fixed intrinsic plastic anisotropy, textures E, F, and G exhibit a higher propensity to void growth $\left(h_{tensile} < 2\right)$ compared to a plastically isotropic material. On the other hand, textures A and D indicate a higher resistance to damage by porosity evolution than the other textures. Such an assessment would not be possible from the compressive AED data if they were to be used as indicators, as they would suggest that all textures being highly susceptible to porosity growth. Hence, one conclusion we make is that for materials such as Mg alloys, it is not advisable to use compression data to characterize this particular mode of damage.

Table 1 Texture cases considered in this work [22]

Angles↓/Cases→	A	B	C	D	E	F	G	H	I	J	K
φ_1^σ	20°	10°	20°	30°	30°	30°	30°	30°	30°	45°	45°
Φ^σ	10°	15°	20°	10°	20°	20°	20°	30°	45°	60°	75°
φ_2^σ	0°	0°	0°	0°	0°	10°	20°	30°	30°	45°	45°
Peak intensity [0001]	31	24	19	30	18	20	18	13	8	6	4
Peak intensity $[10\bar{1}0]$	6	10	6	5	5	5	4	4	3	3	2

Table 2 Material properties for alloyed Mg (AZ31B) alloy and pure Mg (in brackets)

Mechanisms	τ_0(MPa)	h_0(MPa)	τ_s(MPa)		$\tau_0^i/\tau_0^{pris.\langle a\rangle sl.}$
Basal $\langle a\rangle$ slip	10 (0.5)	50 (20)	–		0.18 (0.02)
Prismatic $\langle a\rangle$ slip	55 (25)	1500	110 (85)		1
Pyramidal $\langle a\rangle$ slip	55 (25)	1500	110 (85)		1
Pyramidal $\langle c+a\rangle$ slip	60 (40)	3000	170 (150)		1.09 (1.6)
Extension twinning	τ_0(MPa)	h_{et}(MPa)	τ_{s_et}(MPa)	h_{et_sl}(MPa)	0.27 (0.14)
	15 (3.5)	120 (100)	30 (20)	100	
Contraction twinning	τ_0(MPa)	H_{ct}(MPa)	H_{ct_sl}(MPa)	b	1.55(2.2)
	85 (55)	6000	15	0.05	

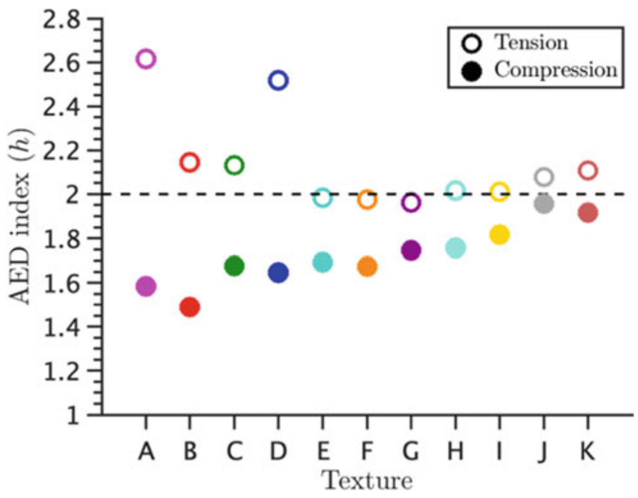

Fig. 3 Steady-state values of the AED index computed for tensile and compressive loading (Mg alloy). The dashed line indicates the limiting case of isotropic plasticity. (Color figure online)

Figure 4 compares the trends of the tensile and compressive AED indices for three textures whose textural intensities are comparable with the experiments of Kondori and Benzerga [14]. As seen, the computed trends are consistent with the particular experimental data.

Shear Anisotropy Ratios

While the compressive AED index is not of much consequence in the context of damage prediction by porosity evolution, the shear anisotropy ratios $(\widehat{h})$ do have relevance in both tension and compression. As noted before, $\widehat{h} \leq 1$ denotes a shear resistant material while $\widehat{h} > 1$ indicates a material that is weak against shear failure. On that backdrop, Fig. 5 reveals some interesting features. Note that the vertical axis is plotted on the logarithmic scale because of the large range of $\widehat{h}$ values particularly in compression. For the given level of crystallographic anisotropy, the propensity of the material to shear instability seems to depend on both, the texture and loading. For a given texture, susceptibility to instability in compression is generally higher than in tension.

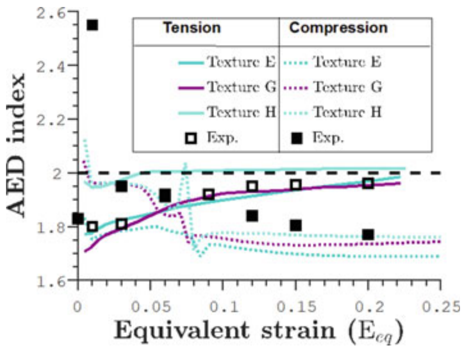

Fig. 4 Comparison of the computed AED index with experimental results [14] for an Mg alloy. The dashed line indicates the limiting case of isotropic plasticity. (Color figure online)

Under tensile loading, stronger textures appear to be more susceptible to shear bands compared to the weaker ones. In general, the $\widehat{h}_{LST}$ correlates with $(10\bar{1}0)$ peak intensity whereas $\widehat{h}_{TSL}$ correlates with (0001) peak intensity in that the higher the peak intensities the higher the corresponding $\widehat{h}$ (i.e. less shear resistant). There appear to be three broad families: (i) weak in shear along both planes comprising textures A and B, (ii) weak in shear along one plane (TS) but shear resistant in the other (LS), comprising textures C, D, and F, and (iii) shear resistant along both planes, comprising textures E, and G-K.

In compression, the situation is more straightforward in that all textures exhibit the propensity to shear bands, although the weaker the texture the lesser its susceptibility to instability compared to the stronger counterparts. Here, both $\widehat{h}_{LST}$ and $\widehat{h}_{TSL}$ appear to correlate better with the between (0001) peak intensity compared to the $(10\bar{1}0)$ peak intensity.

Failure Map

With the foregoing results, we propose a failure map in the $\widehat{h} - h$ space, Fig. 6. The limiting cases for an isotropic material $(\widehat{h} = 1, h = 2)$ split the $\widehat{h} - h$ space into four quadrants. Figure 6a, collates the shear anisotropy data from both tension and compression along both planes and plots it against the tensile AED indices for the same set of textures. The green region is the goldilocks zone; textures whose all four datapoints lie in this zone should be ideal choices in terms of their crystallographic plastic anisotropy and texture. It turns out that for the level of crystallographic anisotropy representative of AZ31B, none of the eleven textures considered here come across as ideal candidates. Several candidates exhibit desirable characteristics insofar as the resistant to porosity evolution is considered but they are expected to generally exhibit poor characteristics against shear failure particularly in compression (northeast). These include: A, B, C, D, H, and I. A few candidates, which occupy the northwest region are altogether undesirable. These comprise: textures E, F, and G. A limited set of textures seem to be somewhat desirable as they occupy the space in the vicinity of the goldilocks zone, e.g. textures J and K.

Notably, the role of compressive loading in shear instability appears crucial. This suggests that the performance of these materials against shear instability in compression is a

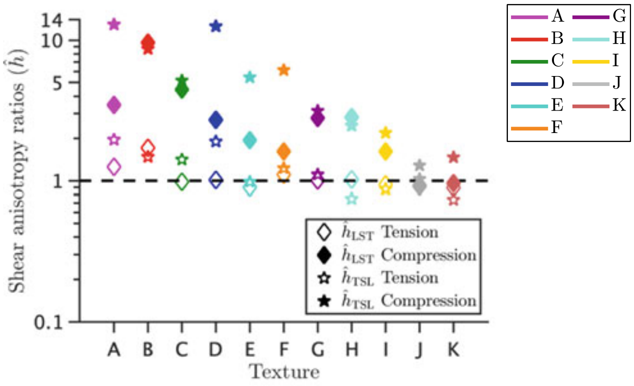

Fig. 5 Texture-dependent steady-state values of shear anisotropy ratios under tensile and compressive loading (Mg alloy). (Color figure online)

factor that may need a deeper investigation. If one ignores the compressive values of $\widehat{h}$, the situation is more forgiving as several textures serve as potential candidates as seen from Fig. 6b.

Role of Crystallographic Anisotropy

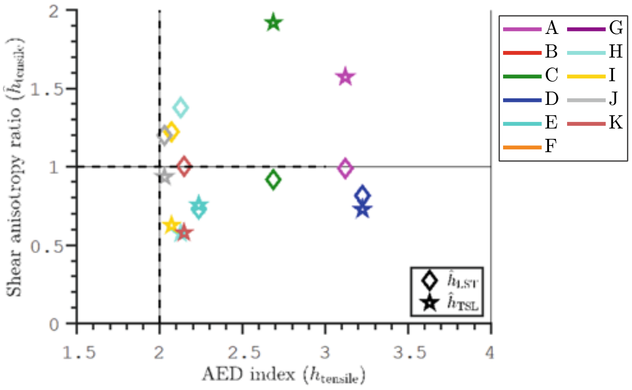

Fig. 7 Failure map for pure Mg. (Color figure online)

We briefly comment on the role of crystallographic plastic anisotropy in the failure landscape. Figure 7 shows the failure map for pure Mg, whose intrinsic crystallographic plastic anisotropy is significantly larger compared to the Mg alloy considered here (cf. Table 2). The figure includes a limited dataset in that only the tensile values of $\widehat{h}$ are plotted and with fewer texture cases (due to much higher computational costs). As seen from the figure, at this level of crystallographic plastic anisotropy there seem to be more possibilities of a damage-tolerant material design. Textures D, E, K exhibit the characteristics of a material that is both, shear resistant and tolerant to internal damage by porosity growth. Even the remaining textures (A, C, H, I, and J) show resistance to porosity growth that is better than an isotropic material and their propensity to shear instability is relatively tempered.

Summary

A predictive understanding of the interacting effects of crystallographic and textural-induced plastic anisotropy in the ductile response of Mg and its alloys is an outstanding challenge. In this work, we present an elementary exploration towards mapping the net plastic anisotropy (derived from crystallographic and texture effects) to the macroscopic damage tolerance against two main agents of ductile failure, porosity growth and shear bands. Motivated by recent proofs of concept, we adopt a simple, yet elegant micromechanical

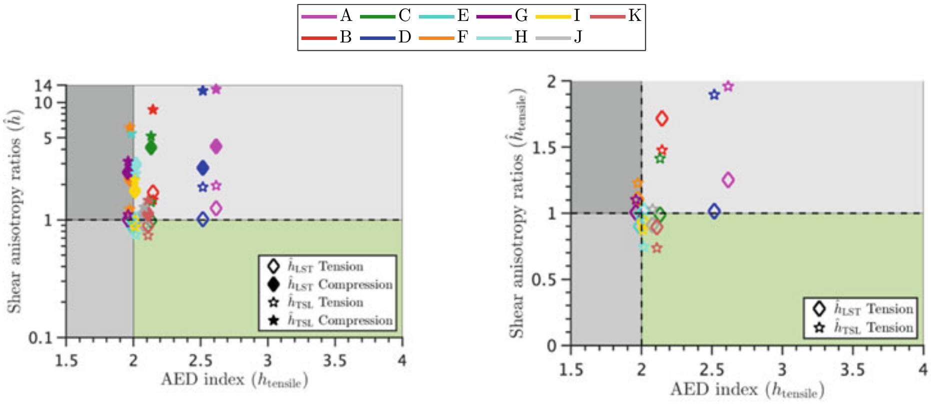

(a) (b)

Fig. 6 Proposed failure map characterized by metrics describing propensity to shear instability $\left(\widehat{\mathrm{h}}\right)$ and damage by porosity evolution (h). Panel (**a**) includes shear anisotropy ratios for both, tension and compression. Panel (**b**) shows the shear anisotropy ratios computed from the tensile dataset only. (Color figure online) model of anisotropic plasticity based on the Hill yield criterion, which delivers the AED index that indicates the effect of plastic anisotropy to porosity growth, and offers insights into potency of shear instability by way of shear anisotropy ratios. Using detailed analysis of the AED indices and shear anisotropy ratios in both tension and compression, we present preliminary failure maps for two levels of crystallographic plastic anisotropies over a wide range of textures. With regard to the questions posed in Introduction, the main observations are as follows:

1. For a material resembling AZ31B Mg, the AED index shows a non-monotonic correlation with textural strengths. The trend suggests that the strongest and the weakest textures may provide a better resistance to porosity driven ductile damage than intermediate textures.
2. On the other hand, for the same material the trends of shear anisotropy ratios suggest that, for tensile loading states, weaker textures may be somewhat more shear resistant compared to stronger and intermediate textures. For compressive loading states, the situation is rather challenging in that most textures may show propensity to shear failure, with the situation being much worse for the strongest textures.
3. For a material with a high crystallographic plastic anisotropy (e.g. pure Mg), the scenario is more forgiving with a wider range of textures showing resistance to both modes of failure.

The analysis presented here needs to be served with caution. While the model has been shown to corroborate with some experimental observations on the anisotropy-ductility linkages in some Mg alloys, it discounts intricacies associated with the crystallographic aspects of deformation mechanisms in Mg that can play a role in the fundamental micromechanics of ductile damage [29]. As such, while the qualitative trends may provide some guidance, a rigorous quantitative assessment may be an overreach. Notwithstanding these caveats, the present work perhaps serves as a preliminary concept towards in silico design of damage-tolerant Mg microstructures guided by the micromechanics of HCP crystal plasticity and coupled into sophisticated homogenization-based mechanics of anisotropic ductile failure.

Acknowledgements SPJ and SB acknowledge financial support from the National Science Foundation, USA under Grant Number CMMI-1932976. PPI is grateful for the support via NUS Research Scholarship. The authors acknowledge the use of the Opuntia Cluster and the advanced support from the Research Computing Data Core at the University of Houston to carry out the research presented here.

References

1. Van der Giessen, E., & Needleman, A. (2002). Micromechanics simulations of fracture. *Annual Review of Materials Research*, *32* (1), 141–162.
2. Besson, J. (2010). Continuum models of ductile fracture: a review. *International Journal of Damage Mechanics*, *19*(1), 3–52.
3. Christian, J. W., & Mahajan, S. (1995). Deformation twinning. *Progress in Materials Science*, *39*(1-2), 1–157.
4. Barnett, M. R. (2007). Twinning and the ductility of magnesium alloys: Part I: "Tension" twins. *Materials Science and Engineering: A*, *464*(1-2), 1–7.
5. Barnett, M. R. (2007). Twinning and the ductility of magnesium alloys: Part II: "Contraction" twins. *Materials Science and Engineering: A*, *464*(1–2), 8–16.
6. Crépin, J., Bretheau, T., & Caldemaison, D. (1996). Cavity growth and rupture of β-treated zirconium: a crystallographic model. *Acta Materialia*, *44*(12), 4927–4935.
7. Kaushik, V., Narasimhan, R., & Mishra, R. K. (2014). Experimental study of fracture behavior of magnesium single crystals. *Materials Science and Engineering: A*, *590*, 174–185.
8. Nemcko, M. J., Li, J., & Wilkinson, D. S. (2016). Effects of void band orientation and crystallographic anisotropy on void growth and coalescence. *Journal of the Mechanics and Physics of Solids*, *95*, 270–283.
9. Huez, J., Helbert, A. L., Feaugas, X., Guillot, I., & Clavel, M. (1998). Damage process in commercially pure α-titanium alloy without (Ti40) and with (Ti40-H) hydrides. *Metallurgical and Materials Transactions A*, *29*(6), 1615–1628.
10. Caré, S., & Zaoui, A. (1996). Cavitation at triple nodes in α-zirconium polycrystals. *Acta Materialia*, *44*(4), 1323–1336.
11. Prasad, N. S., Kumar, N. N., Narasimhan, R., & Suwas, S. (2015). Fracture behavior of magnesium alloys–role of tensile twinning. *Acta Materialia*, *94*, 281–293.
12. Ray, A. K., & Wilkinson, D. S. (2016). The effect of microstructure on damage and fracture in AZ31B and ZEK100 magnesium alloys. *Materials Science and Engineering: A*, *658*, 33–41.
13. Revil-Baudard, B., Cazacu, O., Flater, P., Chandola, N., & Alves, J. L. (2016). Unusual plastic deformation and damage features in titanium: Experimental tests and constitutive modeling. *Journal of the Mechanics and Physics of Solids*, *88*, 100–122.
14. Kondori, B., & Benzerga, A. A. (2014). Effect of stress triaxiality on the flow and fracture of Mg alloy AZ31. *Metallurgical and Materials Transactions A*, *45*(8), 3292–3307.
15. Kondori, B., & Benzerga, A. A. (2015). On the notch ductility of a magnesium-rare earth alloy. *Materials Science and Engineering: A*, *647*, 74–83.
16. Steglich, D., & Morgeneyer, T. F. (2013). Failure of magnesium sheets under monotonic loading: 3d examination of fracture mode and mechanisms. *International Journal of Fracture*, *183*(1), 105–112.
17. Benzerga, A. A., Thomas, N., & Herrington, J. S. (2019). Plastic flow anisotropy drives shear fracture. *Scientific reports*, *9*(1), 1–9.
18. Kondori, B., Morgeneyer, T. F., Helfen, L., & Benzerga, A. A. (2018). Void growth and coalescence in a magnesium alloy studied by synchrotron radiation laminography. *Acta Materialia*, *155*, 80–94.
19. Selvarajou, B., Joshi, S. P., & Benzerga, A. A. (2017). Three dimensional simulations of texture and triaxiality effects on the plasticity of magnesium alloys. *Acta Materialia*, *127*, 54–72.
20. Benzerga, A. A., & Besson, J. (2001). Plastic potentials for anisotropic porous solids. *European Journal of Mechanics-A/Solids*, *20*(3), 397–434.

21. Basu, S., Dogan, E., Kondori, B., Karaman, I., & Benzerga, A. A. (2017). Towards designing anisotropy for ductility enhancement: A theory-driven investigation in Mg-alloys. *Acta Materialia*, *131*, 349–362.
22. Indurkar, P. P., Baweja, S., Perez, R., & Joshi, S. P. (2020). Predicting textural variability effects in the anisotropic plasticity and stability of hexagonal metals: Application to magnesium and its alloys. *International Journal of Plasticity*, 102762.
23. Zhang, J., & Joshi, S. P. (2012). Phenomenological crystal plasticity modeling and detailed micromechanical investigations of pure magnesium. *Journal of the Mechanics and Physics of Solids*, *60*(5), 945–972.
24. Indurkar, PP (2020). On the multiscale mechanics of deformation, stability and damage in magnesium. Ph.D. Thesis, National University of Singapore.
25. Benzerga, A. A., Besson, J., & Pineau, A. (2004). Anisotropic ductile fracture: Part II: theory. *Acta Materialia*, *52*(15), 4639–4650.
26. Benzerga, A. A. (2019). A Theory for Designing Ductile Materials with Anisotropy. In *Magnesium Technology 2019* (pp. 359–362). Springer, Cham.
27. Hill, R. (1948). A theory of the yielding and plastic flow of anisotropic metals. *Proceedings of the Royal Society of London. Series A. Mathematical and Physical Sciences*, *193*(1033), 281–297.
28. Pineau, A., Benzerga, A. A., & Pardoen, T. (2016). Failure of metals I: Brittle and ductile fracture. *Acta Materialia*, *107*, 424–483.
29. Selvarajou, B., Joshi, S. P., & Benzerga, A. A. (2019). Void growth and coalescence in hexagonal close packed crystals. *Journal of the Mechanics and Physics of Solids*, *125*, 198–224.